This is a preprint, the final version is subject to change, of the American Mineralogist (MSA)
Cite as Authors (Year) Title. American Mineralogist, in press.
DOI: https://doi.org/10.2138/am-2019-6564

Revision 1

Sound wave velocities of Fe_5Si at high pressure and high temperature conditions: implications to lunar and planetary cores

Liwei Deng[1,2]*, Yoshio Kono[3], and Guoyin Shen[3]

[1]Key Laboratory of Earth and Planetary Physics, Institute of Geology and Geophysics, Chinese Academy of Sciences, Beijing 100029, China.

[2]University of Chinese Academy of Sciences, Beijing, 100049, China.

[3]HPCAT, Geophysical Laboratory, Carnegie Institution of Washington, Argonne, IL 60439, USA.

*Corresponding author: Liwei Deng (dengliwei@mail.iggcas.ac.cn)

Keywords

Fe-Si alloy, Elastic wave velocity, Lunar and planetary cores, High pressure and temperature

ABSTRACT

Elastic properties of Fe alloys are critical in constraining the compositions of planetary bodies by comparing to the planetary observations. The sound wave velocities and density of an Fe_5Si (9 wt% Si) alloy in body centered cubic (bcc) structure were measured by combining an ultrasonic technique with synchrotron X-ray radiography at pressure (P) and temperature (T) conditions of 2.6-7.5 GPa and 300-1173 K, respectively. At room temperature, it is observed that

adding Si to bcc-Fe increases the compressional wave velocity (V_P) but decreases the shear wave velocity (V_S). At high temperatures, we observed a pronounced effect of pressure on the V_S-T relations in the Fe_5Si alloy. The V_P-density (ρ) relationship of the Fe_5Si alloy is found to follow the Birch's law in the P-T range of this study, whereas the V_S-ρ relation exhibits complex behavior. Implications of these results to the lunar core and the Mercurian core are discussed. Our results imply that adding Si to a pure Fe lunar core would be invisible in terms of V_P, but exhibit a decreased V_S. Including Si in a sulfur-rich lunar core would display an increased V_P and a decreased ρ. Our density and sound wave velocity model provide lower and upper limit for a Si-bearing lunar core if 1-3wt% Si content of Enstatite chondrite is taken as compositional analog. A Si-rich (>9wt %) Mercurian core model is derived to satisfy newly observed moment of inertia values by MESSENGER spacecraft.

INTRODUCTION

It has been widely accepted that the terrestrial planets (such as the Earth and the Mercury) and their satellites (such as the Moon, Konopliv et al. 1998) possess Fe-dominated cores. One or more light elements (such as O, Si, S, C, H) may be present in the cores, based on cosmochemical and geophysical considerations (e.g., Anderson and Ahrens 1994, Anderson and Isaak 2002, Badro et al. 2007). Among the potential light elements, Si remains a dominant candidate, based on several constraints. First, it is experimentally demonstrated that Si has a significant solubility in liquid Fe (25 wt% Si at the eutectic at 21 GPa, Kuwayama and Hirose, 2004) at high pressure and temperature (high P-T) conditions (Fischer et al., 2013). Because magma ocean events, which is characterized by the widespread molten Fe and silicate melt,

might occur in many inner-solar planetary bodies (such as the Mercury and the Earth) and the Moon, the high solubility of Si in liquid Fe provides a mechanism for Si entering into those planetary cores during the silicate-metal differentiation process (Ricolleau et al., 2011, Badro et al, 2015). Second, the siderophile element partitioning data strongly support that early accretion of the Earth and the Mercury occurred under highly reduced conditions (Malavergne et al. 2010, Javoy et al., 2010). Moreover, the Gamma-ray spectrometers of the Mercury's MESSENGER spacecraft revealed that an amount of 1-4wt% S could be present on the Mercury's surface, implying that the oxygen fugacity of the Mercury's interior is rather low, with an IW ranging from -2.6 to -7.3 (Chabot et al., 2014). The extremely low oxygen fugacity is compatible with the reduced nature of Si. Thus substantial Si could have been incorporated into the cores during the core-mantle segregation.

Pure iron adopts at least three polymorphs at high P-T, including body-centered-cubic (bcc), face-centered-cubic (fcc), and hexagonal-closed-packing (hcp). The fcc- and hcp-Fe are commonly viewed to be the dominant phases at terrestrial planetary cores, because of their stability fields of the related P-T conditions. However, high pressure experimental and theoretical studies suggested that the addition of Si or Ni in Fe can stabilize the bcc structure at expanded P-T conditions (Lin et al., 2002, Dubrovinsky et al., 2007, Vocadlo et al., 2008, Kuwayama et al., 2009). For example, in situ X-ray diffraction experiments on an $Fe_{5.3}Si$ alloy found a stabilized mixture of bcc and hcp phases up to at least 150 GPa and 3000 K (Lin et al., 2009). Therefore, a bcc structured Fe-Si alloy could be a candidate phase in the cores of terrestrial planets and their satellites.

Sound wave velocity is a critical physical parameter for constraining the planetary core compositions. In conjunction with the seismological observations of the planetary interior, it

provides a direct approach to model the nature of the inaccessible planetary interiors. Multiple techniques, including ultrasonic techniques, shock compression, high-energy resolution inelastic X-ray scattering (HERIXS), and nuclear resonant inelastic X-ray scattering (NRIXS), have been adapted to measure V_P and V_S mostly on hcp- and fcc-Fe and their alloys by several groups (Fiquet et al., 2001, Mao et al., 2001, Lin et al., 2005, Badro et al., 2007, Mao et al., 2012, Antonangeli et al., 2004, 2015a, b, 2018). HERIXS technique can probe the momentum-resolved phonon dispersions, from which V_P is fitted. And V_S is derived by combining the measured V_P and equation of state (density and adiabatic bulk modulus). The resultant sound velocity depends strongly on how well the data sample the linear part of the phonon dispersion and on the knowledge of sample texture (Antonangeli and Ohtani 2015b). The NRIXS method provides information of partial phonon density of states (pDOS), through which the Debye sound velocity can be obtained. Together with information of density and adiabatic bulk modulus, V_P and V_S can then be determined (Shen and Mao, 2017). In shock experiments, temperature is not well determined, and is tied with pressure along a Hugoniot. The ultrasonic method is a direct way to measure V_P and V_S at high P-T conditions (Urick 1947). This method has been recently successfully used in conjunction with X-ray synchrotron radiation, providing insightful information of V_P and V_S of several geophysical important materials at high P-T (Higo et al., 2009, Kono et al., 2010, 2012, Li et al., 2007, 2014).

Sound wave velocity measurements on bcc Fe-Si alloys are relatively few. The only available sound wave velocity data were V_P of a $Fe_{5.3}Si$ alloy reported by Lin et al. (2003a) by NRIXS and Liu et al. (2014) by HERIXS measurements. Notably, there is an approximately 10% difference between their V_P results, although the same stoichiometric samples with $Fe_{5.3}Si$ were used in these two studies. Moreover, these two measurements were conducted only at room temperature.

Temperature effect on sound wave velocities of bcc Fe-Si alloys is still unknown. In this study, we have conducted ultrasonic measurements on a bcc Fe_5Si sample at simultaneous high P-T conditions. We present the effect of Si on V_P and V_S of the bcc Fe-Si alloy at high P-T conditions. The implications of these observations for the planetary core compositions are discussed.

EXPERIMENTS

High P-T ultrasonic velocity measurements were conducted using a Paris-Edinburgh press at the 16-BMB station at the Advanced Photon Source, Argonne National Laboratory (Kono et al., 2012). The Fe_5Si powder, from Goodfellow, was hot-pressed in a piston-cylinder apparatus at 1 GPa and 1073 K for 2hrs. The hot-pressed Fe_5Si disk size was about 1.5 mm (diameter) × 0.8~1.2 mm (length). Mirror-finished sample surfaces were produced by carefully polishing using 1 μm diamond paste. A schematic illustration of the cell assembly is shown in Figure 1. Pressures were determined by X-ray diffraction of Au using the equation of state by Tsuchiya et al. (2003). The static pressures were evaluated based on second-order Birch-Murnagham Equation of State. And thermal pressures were calculated based on Mie-Grüneisen equation ($\mathrm{Pth} = \frac{\mathrm{r}*\mathrm{Eth}}{\mathrm{v}}$, where Pth and Eth are thermal pressure and energy, respectively. r is Grüneisen parameter and v is volume. Eth is evaluated based on Debye model). The typical errors in pressure are 2-8%. The sample was heated in a graphite cylinder, with temperatures estimated from a previously calibrated power-temperature curve with an identical assembly (Jing et al., 2014). The temperature uncertainties are about 100 K. The experimental P-T conditions were 2.6-7.5 GPa and 300-1173 K, respectively. For each run, we compressed the sample to a target pressure and then increased temperature. At any given temperature we waited approximately 1-

2mins before collecting ultrasonic, X-ray radiography, and X-ray diffraction data, in order to reduce the deviatoric stress imposed on the sample during compression.

At each specified P-T conditions, ultrasonic interference and radiographic imaging techniques allow simultaneous determination of travel time and sample length respectively, from which sound velocities were yielded. Figure 2 shows an example of the P- and S-wave signals obtained at 2.6 GPa and 985 K. 30 MHz and 20 MHz electrical sine waves were generated for V_P and V_S measurements, respectively. They propagate into sample assembly and reflected at the interfaces, which were labeled as R_0 (anvil/Al_2O_3), R_1 (Al_2O_3/Fe_5Si sample) and R_2 (Fe_5Si sample/BN). Then the travel time for the sound velocity can be determined by difference of arrivals of R_1 and R_2. The uncertainty in the travel time is within ±0.1ns, corresponding to less than 0.1% uncertainties in V_P and V_S, respectively. The sample lengths under high P-T were measured from an X-ray radiography image using a high-resolution CCD camera (Kono et al., 2012). The pixel resolution was 0.948μm/pixel. The error on the measured sample length is less than 1μm. The resultant uncertainty introduced by sample length measurements for elastic waves is less than 0.03% and 0.18% at 300 K and high T, respectively.

RESULTS AND DISCUSSION

Equations of state

$Fe_{5.2}Si$ is considered to adopt the $D0_3$ crystal structure (cubic, space group: Fm3m, 225) at ambient conditions (Massalski, 1986) and under compression at 300 K to at least 29 GPa (Fischer et al., 2013). Our room temperature data show that this alloy maintains a bcc structure with a different space group (Im3m, 229) at 3.6-7.5 GPa (Figure 3). It may be related to the high P-T synthesis conditions (1 GPa and 1073 K for 2hrs). Fischer et al. (2013) found that the Fe_5Si alloy would convert into an fcc+B_2 mixture above 10 GPa and 1000 K. In the P-T range of this

study up to 6.1 GPa and 1173 K, we did not observe any diffraction peaks corresponding to either the fcc or the B_2 phase. Our data show that the Fe_5Si alloy adopts a bcc structure throughout our experimental P-T conditions.

The unit-cell volumes were obtained simultaneously together with the elastic velocity measurements, with the results summarized in Table 1. The obtained pressure-volume data at 300 K were fitted into the second-order Birch-Murnaghan equation of state (EOS). The resultant isothermal bulk modulus (K_{T0}) and volume (V_0) are 188 (18) GPa and 23.2(2) $Å^3$, respectively. In addition, the thermal expansion coefficient (α_T) over a temperature range of 800-1154 K at 2.6 GPa is $5.27(4.0)\times10^{-5}$ K^{-1}. Our α_T and V_0 are in general agreement with those by Zhang et al. (1999) ($\alpha_T=4.74\times10^{-5}$ K^{-1}, $V_0=23.0$ $Å^3$), while K_{T0} is relatively larger than Zhang's results (K_0=161GPa).

V_P and V_S at 300 K

Figure 4 shows V_P and V_S of the bcc Fe_5Si alloy and pure Fe at room temperature as a function of pressure. Our V_P results are consistent with those of Liu et al. (2014) by HERIXS, but larger than those of Lin et al. (2003a) by NRIXS. Similarly, it has been known that the V_P of bcc-Fe is also consistent between ultrasonic (Shibazaki et al., 2016, Chigarev et al., 2008, Fiquet et al., 2001) and HERIXS measurements (Liu et al., 2014). Because NRIXS measures Debye sound velocity (V_D), and calculate V_P and V_S based on ρ and bulk modulus determined in separate experiments, the inconsistency of the results from the NRIXS measurement may be due to the indirect approach. Our study, together with the results of Liu et al. (2014), supports that alloying Si in bcc-Fe increases V_P at room temperature.

158 The available S-wave data of bcc-Fe and Fe-Si alloys are limited. The only available S-wave
159 data of a $Fe_{5.3}Si$ alloy was the NRIXS results by Lin et al. (2003a). Our obtained V_S are slightly
160 larger than that of Lin et al. (2003a), with both data sets displaying lower V_S than that of bcc-Fe
161 (Shibazaki et al., 2016, Chigarev et al., 2008). It needs to be pointed out that due to the poor
162 signal-to-noise ratio, probably arising from small acoustic reflection coefficient between the
163 Al_2O_3 buffer rod and the bcc-Fe_5Si sample, only one data point of V_S was obtained at room
164 temperature in this study. At room T, acoustic impedance for V_S of the Fe_5Si sample is ~25 at 7.7
165 GPa, which is similar to that of the buffer rod Al_2O_3 (~25, e.g., Kung et al., 2000). Nevertheless,
166 at high temperatures, this situation was improved, because the V_S of the Fe_5Si sample decreases
167 significantly, with reduced acoustic impedances and improved signals in acoustic reflections.

168 **Temperature dependence of V_P and V_S**

169 Liu et al. (2014), Shibazaki et al. (2016) and Antonangeli et al. (2015a) have investigated the
170 effect of temperature on V_P and V_S of bcc-Fe under compression, as shown in Figure 5. In bcc-
171 Fe, both V_P and V_S decrease with increasing temperature. The temperature dependences of V_P
172 and V_S under different pressures remain almost the same in a temperature range of 300-700 K.
173 These results for bcc-Fe are compared with our high temperature results of V_P and V_S for the
174 Fe_5Si sample at 2.6-6.1 GPa (Figure 5). It shows that in the Fe_5Si alloy the temperature
175 dependence of V_S is much stronger than that of V_P at a given pressure. For example, at 2.6 GPa
176 with a temperature decrease of 354 K, $\triangle V_P$ is only 4.9%, compared to a $\triangle V_S$ of 20.4% in the
177 Fe_5Si alloy.

178 Meanwhile, the temperature dependence of V_S in the bcc Fe_5Si sample weakens as pressure is
179 increased, which is in contrast to the temperature independence of V_S in bcc-Fe with varying
180 pressure. For example, with the same temperature interval (ΔT=350K), $\triangle V_S$ is 5.3% in bcc-Fe at

2-2.7 GPa, 4-4.5 GPa and 5.4-5.8 GPa (Shibazaki et al., 2016), while $\triangle V_S$ in the Fe_5Si sample is ~20% and ~10% at 2.6 GPa and 5.5-6.1 GPa, respectively. Temperature dependence of V_P can not be assessed since our present data are at one pressure.

Applicability of the Birch's law

The Birch's law suggests that the sound wave velocity of rocks is mainly a function of ρ and mean atomic weight: $V=a(m)+b\times\rho$, where a and b are Birch's constants and m is the mean atomic weight (Birch 1960). On the other hand, the validity of the Birch's law for different Fe phases is still under debate. Antonangeli et al. (2010, 2015a, 2015b) reported that bcc, fcc and hcp Fe phases follow a linear V_P-ρ relation over their investigated P-T ranges (0-19 GPa, 300-1150 K). In contrast, Shibazaki et al. (2016) showed that the V_P-ρ relation depends on temperature for bcc-Fe at 2-6.3 GPa and 300-814 K. Figure 6a shows our V_P-ρ data collected at 2.6-7.5 GPa and 300-1154 K, together with previous reported V_P-ρ datasets. Our data show a linear V_P-ρ relation for bcc Fe_5Si not only at room temperature condition but also at high temperature conditions: $V_P=1.32\times\rho-3.49$ ($R^2=0.99$). Thus our results confirmed the validity of Birch's law for Fe-Si alloy over the P-T range of this study. The Birch's law seems to hold for the rest components as shown in figure 6a regardless of the phases and applied experimental temperatures in a broad density range. The only exception is bcc iron ($R^2=0.86$), discussed by Shibazaki et al. (2016).

On the other hand, V_S-ρ data for bcc-Fe and Fe-Si alloys are few and appear to be more complex (Figure 6b). It shows that our 300 K point is consistent with Lin's (2003a) room T data but far from the rest high temperature V_S data. The possible reason for the large derivation is that

204 temperature might have a fundamentally important effect on V_S. Similar observation has been
205 made by Shibazaki et al. (2016) that in bcc-Fe V_S strongly depend not only on density but also
206 on temperature. Therefore, cautions must be taken when applying the Birch's law for V_S.

207 **IMPLICATIONS TO THE SOUND WAVE VELOCITY MODELS OF THE LUNAR**
208 **AND MERCURIAN CORES**

209 Growing evidence suggests that the terrestrial planets and their satellites, such as the Mercury,
210 the Earth and the Moon, share lots of similarities in many ways, such as the layered structures
211 and the elements variety (Brown and Elkins-Tanton 2009, Lin et al., 2016). Si is suggested to be
212 a highly potential light element at the P-T conditions of the cores of the Earth (125-350 GPa,
213 3000-6000 K, Wänke and Dreibus 1997) and the Mercury (8-40 GPa, 1700-2200 K, Chabot et
214 al., 2014) based on geophysical and geochemical constraints. There is no direct evidence yet that
215 Si may exist in the lunar core (5-6GPa, 1300-1900 K, Wieczorek 2006). However, according to
216 giant impact theory, the Moon might form from similar building blocks to that of the Earth, as
217 demonstrated by isotopic evidences including oxygen, chromium and titanium (Dauphas 2017).
218 Enstatite chondrite meteorites may represent possible building blocks of the Earth-Moon system
219 as they have almost indistinguishable isotopic compositions (Qin et al., 2010, Javoy et al., 2010,
220 Warren et al., 2011, Zhang et al., 2012, Young et al., 2016). Fe-Ni is an abundant mineral in
221 Enstatite chondrite and 1-3wt% Si is being found in Fe-Ni metal solution (Mason 1966).
222 Therefore, Si might be an important light element in lunar core, as suggested for the Earth
223 (Antonangeli et al., 2010).

224 Here we calculated V_P and V_S of our 9 wt% Si and 91 wt% Fe sample under the P-T
225 conditions of the Mercury and Lunar cores. The high P-T sound wave velocity is calculated as:

226 $$V = V_{(P,300K)} + (\frac{dV}{dT})_P \times \Delta T \ ,$$

where $V_{(P,300K)}$ and $(\frac{dV}{dT})_P$ are the elastic wave at high pressure and 300 K and temperature dependence of elastic wave, respectively. First, we extrapolated the sound wave velocity to the target pressure using $V_{(\text{P-wave},300\text{K})} = 0.04(1)\times P + 6.34(1)\left(R^2 = 0.98\right)$ and $V_{(\text{S-wave},300\text{K})} = 0.032(1)\times P + 2.99(2)(R^2=0.91)$, which were derived by fitting our datasets (Figure 1). As only one data point of V_S is available at 300 K, the slope of V_S-P relation from Lin et al. (2003) was used to construct $V_{(\text{S-wave},300\text{K})} - P$ relations, i.e. $V_{(\text{S-wave},300\text{K})} = 0.032(1)\times P + 2.99(2)(R^2=0.91)$. Secondly, temperature effect was evaluated through $\left(dV_P / dT\right)_{2.6\text{GPa}} = -0.0008(1)\ \text{km/s}\ \left(R^2 = 0.89\right)$ and $\left(dV_S / dT\right)_{5.5\text{GPa}} = -0.00097\ \text{km/s}$, which were derived by fitting our high temperature V_P and V_S data at temperature ranges of 800-1154 K and 854-1173 K, respectively. Based on our sound wave velocity data, the estimated V_P and V_S profiles, together with ρ profiles for the interiors of the Moon and the Mercury are shown in Figures 7-8.

Due to the paucity of seismic waves that penetrate the deepest 500 km of the Moon identified in the Apollo seismic data, the composition and status constraints on deep lunar interior are insufficiently known at present. At present most the lunar interior density and sound wave velocity models only consider S as a light element in the solid inner core or a pure fcc Fe core. The density and sound wave velocity models of a Si constituent solid inner core have not been developed yet. For example, Weber et al. (2011) assumed V_P and V_S to be 4.2 km/s and 2.2 km/s for a S-rich solid inner core based on high pressure elasticity measurements of iron alloys (Sanloup et al., 2000, Williams 2009, Balog et al., 2003). In contrast, based on an fcc Fe lunar inner core model, Antonangeli et al. (2015a) proposed that V_P and V_S should be 4.7-5.7 km/s and

248 2.1-3.4 km/s, respectively. Based on the experimental results of this study, a Si-rich lunar inner
249 core would possess following characteristics compared to a pure Fe or a S-rich lunar core (Figure
250 7): V_P and ρ of a Si-rich core is comparable and slightly smaller than their counterparts in a pure
251 Fe core, respectively. A Si-rich core has much higher V_P and moderately smaller ρ than those of
252 a S-rich core. V_S of a Si-rich core are relatively smaller than those of a pure Fe and S-rich cores
253 (Figure 7). It has been established in the Fe-rich Fe-Si alloy the density and sound wave velocity
254 decrease and increase respectively with increasing Si content at 300 K (Lin et al., 2003b). Our
255 proposed models were built based on the assumption that lunar core contains 9 wt% Si. If Fe-Ni
256 metal alloy in Enstatite chondrite, which contains 1-3wt% Si, is taken as composition analogy of
257 the lunar core. Then our present model (Figure 7) provides lower and upper values for density
258 and sound wave velocity respectively in a 1-3wt% Si-bearing core, assuming thermal expansion
259 and $\left(dV/dT\right)$ at lower Si content (1-3wt%) are comparable to their counterparts at 9 wt% Si
260 content. It should be note that moon might form under relatively more oxidized condition (IW-1,
261 Jones and Palme, 2000) compared to fO_2 values of Enstatite chondrite(IW-3 to -8, McCoy et al.,
262 1999), which indicates less Si (<1-3wt%) entered into lunar core during core-mantle segregation.
263 However, reducing Si concentration in Fe-Si alloy will result in larger density and smaller sound
264 velocity. Therefore, the constraints of lowers values for density and upper values for sound wave
265 velocity are still valid in a less Si-bearing (<1-3wt%) lunar core.

266 As the innermost and the second densest planet of the solar system, the Mercury holds a
267 crucial position in understanding the formation and the evolution of the terrestrial planets.
268 Constraints on the composition and interior structure of the Mercury mainly come from
269 observations of MARINER 10 and MESSENGER spacecrafts. An intrinsic magnetic field in the
270 Mercury is among major accomplishments of these two missions, and it brought up the idea that

the Mercury should have a core which might be partially molten (our experimental data were collected in solid phase zone, hereafter discussions and models are specifically for Mercurian solid inner core only). Knibbe and Westrenen (2015, 2018) conducted a series of studies to investigate the thermal and magnetic field evolution of a Fe-Si alloy Mercurian core. Their results indicate that a Si dominated Mercurian core is highly possible. In such a Fe-Si core, no compositional convection is generated upon core solidification, in agreement with magnetic field indications of a stable layer at the top of the Mercury. Moreover, a Si-bearing core has the advantage to explain the highly reduced nature in the Mercury, as opposed by a Fe-S core. We calculated density and sound wave velocity of the Fe_5Si alloy at pressure and temperature conditions corresponding to the interior of the Mercury (Figure 8). By comparing our measured ρ between 300 K and 1700 K (estimated T at the Mercury's CMB) together with EOS measurements of 16wt% Si (Fischer et al., 2013), it clearly shows that the Si content has a much stronger effect on ρ than temperature. To our best knowledge, only two literatures, which were both published by Knibbe and Westrenen (2015, 2018), specifically studied and yielded the interior density models for a Si-bearing Mercurian core. Polar moment of inertia (C/MR^2) and fraction of polar moment of outer solid shell (C_m/C) are two important parameters to constrain the density distribution of the Mercury's interior in particular. Knibbe and Westrenen (2015, 2018) calculated a large number of Mercury's density profiles as a function of Si content using Monte Carlo approach. And corresponding C/MR^2 and C_m/C were calculated for each density profiles. To satisfy the newly updated C/MR^2 and C_m/C values by radio tracking data from the MESSENGER spacecraft (Mazarico et al., 2014, Stark et al., 2015), Knibbe and Westrenen estimated the average density to be 6.5~7.5g/cm^3 in a Si-bearing Mercurian core. And they proposed the corresponding Si content, respectively, to be 20 wt% and 7 wt%. Figure 8a shows

that their density profiles of 7 wt% and 20 wt% Si are systematically lower than those from Fisher et al. (2013) and the results of this work. Two possible sources may contribute to this discrepancy. First, the density profiles in Knibbe and Westrenen (2018) were interpolated and extrapolated linearly based on EOS parameters of pure fcc Fe (Komabayashi and Fei, 2010) and $Fe_{71}Si_{29}$ (~17 wt% Si) (Lin et al., 2003b). The effect of temperature on EOS of $Fe_{71}Si_{29}$ was not taken into account. Secondly, $Fe_{71}Si_{29}$ is in B2 phase in Lin's (2003b) studied P-T range, which will make it difficult to inter/extrapolate with a phase in different structure (fcc-Fe). In order to satisfy density constraints of 6.5~7.5g/cm^3, our results suggest a Si content in the Mercurian core higher than 9 wt%. In Figure 8a, density profiles of $Fe_{2.6}Si$ (16 wt% Si, Fischer et al., 2013) at 300 K and 1700 K (α_T of $Fe_{2.6}Si$ sample is unknown, we used α_T of Fe_5Si sample instead to correct the density of $Fe_{2.6}Si$ sample to high T) were shown as well. A Si abundant (>16 wt%) Mercurian core could even be possible given the EOS measurements and high-T density corrections were correct. Presently, direct observation on Mercurian core composition is not possible. Sound wave velocity models for Mercurian core are quite few and mostly from elastic wave measurements and thermodynamic calculations. Figure 8b compared the sound wave velocity models of a Fe-Ni (10% Ni by weight) alloy core (thermodynamic model by Lv et al., 2011), a pure fcc Fe core (High P-T measurements by Antonangelia et al., 2015a) and a Fe-Si alloy core (9% Si by weight) (this work). It shows that incorporating Ni in pure Fe results in an increased sound wave velocity while adding Si has the opposite effect. Moreover, even the similar amount of light element influence the sound wave velocity to quite different extent. For example, additional 10 wt% Ni in pure fcc Fe result in 18~19% increment in both V_P and V_S. While V_P and V_S with additional 9 wt% Si are about 6.4 % and 43 % smaller than that of a pure fcc Fe, respectively.

Comparing laboratory measured density and sound wave velocity values with planetary observation data is a direct approach to constrain the deep interior status and compositions. For the moon, our study shown that a Si-rich lunar core exhibits comparable V_P and different V_S in contrast to pure Fe core or S-rich core. This observation stresses the importance of simultaneous match of V_P and V_S when constraining lunar core composition use seismograms data and high pressure elastic data. Present seismic data of lunar core are from Apollo mission and far less than that required to constrain the interiors. However, international community has shown long term ambitions to explore outer space and great achievements have been made. For example, China's series of Chang'e Moon missions have sent spacecraft to lunar orbit and the lunar surface. Seismometer deployment on the lunar surface is also being planned around 2025. Laboratory proposed sound wave velocity models, including ours, are likely to be testable by the upcoming missions.

For the Mercurian core, our study suggests a large amount (>9 wt% or even higher than 16 wt%) of Si might be in it to best satisfy moment of inertia constraints. As mentioned before, there is no direct seismic observation of Mercurian core. Highly reduced Aubrite meteorites is a potentially relevant analog given Mercurian highly reduced nature (i.e. IW-3 to IW-7). It contains an average of 0.1-2.4 wt% Si (Mt. Egerton has the largest amount of Si in the metal of 4 wt%). High P-T experimental studies has well established that Si become more siderophile under more reducing conditions (i.e. Si changes from lithophile to siderophile at IW-3.5, Corgne et al., 2008). Therefore, a large amount of Si could enter the Mercurian core during magma ocean process, which is consistent with our suggested Si-bearing model. It should be note that our proposed Si content in Mercurian core composition is derived based on extrapolation of relatively low experimental pressures in contrast to Mercurian core. At characteristic Mercurian

core pressure condition, Fe_5Si sample of bcc phase might convert into more complex phases (i.e. fcc+B2 or hcp+B2) as suggested by Fischer et al. (2013). However, either fcc or hcp phases are denser than bcc. Therefore, even more Si is required in the Mercurian core to satisfy density constraints.

Systematic elastic data, especially sound wave velocity, at characteristic lunar and planetary core P-T conditions for a broader selective light element (such as C, S, O, H) are quite scarce. We still need further experimental work on high P-T EOS and elastic property measurements for Fe-multiple light elements system. In all, density and sound wave velocity data, combined with spacecraft observations, are critical for further refining the elastic property of core materials, which will provide tight constraints on the composition and evolution of the planetary and lunar interiors.

ACKNOWLEDGMENTS

This work was supported by the National Natural Science Foundation of China (41374096, 41174071), the Strategic Priority Research Program (B) of the Chinese Academy of Sciences (XDB18000000) and the Major Program of National Natural Science Foundation of China (41490630). This work was performed at HPCAT (Sector 16), Advanced Photon Source (APS), Argonne National Laboratory. GS and YK acknowledge the support by DOE-BES, Division of Materials Sciences and Engineering under Award No. DEFG02-99ER45775. HPCAT operation is supported by DOE-NNSA under Award No. DE-NA0001974, with partial instrumentation funding by NSF. The Advanced Photon Source is a U.S. Department of Energy (DOE) Office of Science User Facility operated for the DOE Office of Science by Argonne National Laboratory under Contract No. DE-AC02-06CH11357.

REFERENCES CITED

Anderson, W. W., and Ahrens, T. J. (1994) An equation of state for liquid iron and implications for the Earth's core. Journal of Geophysical Research, 99, 4273-4284.

Anderson, O. L., and Isaak, D. G. (2002) Another look at the core density deficit of Earth's outer core. Physics of the Earth and Planetary Interiors, 131, 19-27.

Antonangeli, D., Siebert, J., Badro, J., Farber, D. L., Fiquet, Morard, G., and Ryerson, F. J. (2010) Composition of the Earth's inner core from high pressure sound velocity measurements in Fe-Ni-Si alloys. Earth and Planetary Science Letter, 295, 292-296.

Antonangelia, D., Morarda, G., Schmerr, N. C., Komabayashi, T., Krisch, M., Fiquet, G., and Fei, Y. W. (2015a) Toward a mineral physics reference model for the Moon's core. Proceedings of the National Academy of Sciences. USA, doi/10.1073.

Antonangeli, D., and Ohtani, E. (2015b) Sound velocity of hcp-Fe at high pressure: experimental constraints, extrapolations and comparison with seismic models. Progress in Earth and Planetary Science, DOI 10.1186/s40645-015-0034-9.

Antonangeli, D., Occelli, F., Requardt, H., Badro, J., Fiquet, G., and Krisch, M. (2004) Elastic anisotropy in textured hcp-iron to 112 GPa from sound velocity wave propagation measurements. Earth and Planetary Science Letters, 225, 243-251.

Antonangeli, D., Morard, G., Paolasini, L., Garbarino, G., Murphy,, C. A., Edmund, E., Decremps, F., Fiquet, G., Bosak, A., Mezouar, M., and Fei, Y. W. (2018) Sound velocities and density measurements of solid hcp-Fe and hcp-Fe–Si (9 wt.%) alloy at high pressure: Constraints on the Si abundance in the Earth's inner core. 482, 446-453.

384 Badro, J., Brodholt, J. P., Piet, H., Siebert, J., and Ryerson, F. J. (2015) Core formation and
385 core composition from coupled geochemical and geophysical constraints. Proceeding of the
386 National Academy of Sciences, 112, 12310-12314.
387 Badro, J., Fiquet, G., Guyot, F., Gregoryanz, E., Occelli, F., Antonangeli, D., and d'Astuto, D.
388 (2007) Effect of light elements on the sound velocities in solid iron: implications for the
389 composition of Earth's core. Earth and Planetary Science Letters, 254, 233-238.
390 Balog, P. S., Secco, R. A., Rubie, D. C. and Frost, D. J. (2003) Equation of state of liquid Fe-
391 10wt% S: Implications for the metallic cores of planetary bodies. Journal of Geophysical
392 Research, 108, NO. B2, 2124.
393 Birch, F. (1960) The velocity of compressional waves in rocks to 10 kilobars. Part 1, Journal
394 of Geophysical Research, 65, 1083-1102.
395 Brown, S., and Elkins-Tanton, L. T. (2009) Compositions of Mercury's earliest crust from
396 magma ocean models. Earth and Planetary Science Letters, 286, 446-455.
397 Chabot, N. L., Wollack, E. A., Klima, R. L., and Minitti, M. E. (2014) Experimental
398 constraints on Mercury's core composition. Earth and Planetary Science Letters, 390, 199-208.
399 Chigarev, N., Zinin, P., Ming, L. C., Amulele, G., Bulou, A. and Gusev, V. (2008) Laser
400 generation and detection of longitudinal and shear acoustic waves in a diamond anvil cell.
401 Applied Physics Letters, 93, 181905.
402 Corgne, A., Keshav, S., Wood, B. J., McDonough, W. F., and Fei, Y. (2008) Metal-silicate
403 partitioning and constraints on core composition and oxygen fugacity during Earth accretion.
404 Geochimica Cosmochimica Acta, 72, 574-589.
405 Dauphas, N. (2017) The isotopic nature of the Earth s accreting material through time. Nature,
406 541, 521-524.

Dubrovinsky, L., Dubrovinskaia, N., Narygina, O., Kantor, I., Kuznetzov, A., Prakapenka, V. B., Vitos, L., Johansson, B., Mikhaylushkin, A. S., Simak, S. I., and Abrikosov, I. A. (2007) Body-centered cubic iron-nickel alloy in Earth's core. Science, 316, 1880-1883.

Fiquet, G., Badro, J., Guyot, F., Requardt, H., and Krisch, M. (2001) Sound velocities in iron to 110 Gigapascals. Science, 291, 468-471.

Fischer, R. A., Campbell, A. J., Reaman, D. M., Miller, N. A., Heinz, D. L., Dera, P. L., and Prakapenka, V. B. (2013) Phase relations in the Fe-FeSi system at high pressures and temperatures. Earth and Planetary Science Letters, 373, 54-64.

Higo, Y., Kono, Y., Inoue, T., Irifune, T., and Funakoshi, K. (2009) A system for measuring elastic wave velocity under high pressure and high temperature using a combination of ultrasonic measurement and the multi-anvil apparatus at SPring-8. Journal of synchrotron radiation, 16, 762-768.

Javoy, M., Kaminski, E., Guyot, F., Andrault, D., Sanloup, C., Moreira, M., Labrosse, S., Jambon, A., Agrinier. P., Davaille, A., Jaupart, C. (2010) The chemical composition of the Earth: Enstatite chondrite models. Earth and Planetary Science Letters, 293, 259-268.

Jing, Z. C., Wang, Y. B., Kono, Y., Yu, T., Sakamaki, T., Park, C., Rivers, M. L., Sutton, S. R., and Shen, G. Y. (2014) Sound velocity of Fe-S liquids at high pressure: Implications for the Moon's molten outer core. Earth and Planetary Science Letters, 396, 78-87.

Jones, J. H. and Palme, H. (2000) Geochemical constraints on the origin of the Earth and Moon. In Origin of the Earth and Moon (eds. R. M. Camp and K. Righter). University of Arizona Press, Tucson, pp. 197-216.

Kantor, A. P., Kantor, I. Y., Kurnosov, A. V., Kuznetsov, A. Y., Kuznetsov, A. Y., Dubrovinskaia, N. A., Krisch, M., Bossak, A. A., Dmitriev, V. P., Urusov, V. S. and

Dubrovinsky, L. S. (2007) Sound wave velocities of fcc Fe-Ni alloy at high pressure and temperature by mean of inelastic X-ray scattering. Physics of the Earth and Planetary Interiors, 164, 83-89.

Knibbe, J. S., and Westrenen, W. V. (2015) The interior configuration of planet Mercury constrained by moment of inertia and planetary contraction. Journal of Geophysical Research: Planets, 120, 1904-1923, doi:10.1002/2015JE004908.

Knibbe, J. S., and Westrenen, W. V. (2018) The thermal evolution of Mercury's Fe–Si core. Earth and Planetary Science Letters, 482, 147-159.

Komabayashi, T., and Y. Fei (2010) Internally consistent thermodynamic database for iron to the Earth's core conditions. Journal of Geophysical Research Solid Earth, 115, B03202, doi:10.1029/2009JB006442.

Kono, Y., Irifune, T., Higo, Y., Inoue, T., and Barnhoorn, A. (2010) P-V-T relation of MgO derived by simultaneous elastic wave velocity and in situ X-ray measurements: A new pressure scale for the mantle transition region. Physics of the Earth and Planetary Interiors, 183, 196-211.

Kono, Y., Park, C., Sakamaki, T., Kenny-Benson, C., Shen, G., and Wang, Y. (2012) Simultaneous structure and elastic wave velocity measurement of SiO_2 glass at high pressures and high temperatures in a Paris-Edinburgh cell. The Review of Scientific Instruments, 83, 033905.

Konopliv, A. S., Binder, A. B., and Hood, L. L. (1998) Improved gravity field of the Moon from Lunar prospector. Science, 281, 1476-1480.

Kung, J., Rigden, S., and Gwanmesia, G. (2000) Elasticity of $ScAlO_3$ at high pressure. Progress in Earth and Planetary Science, 118, 65-75.

Kuwayama, Y., and Hirose, K. (2004) Phase relations in the system Fe-FeSi at 21 GPa. American Mineralogist, 89, 273-276.

Kuwayama, Y., Sawai, T., Hirose, K., Sata, N, and Ohishi, Y. (2009) Phase relations of iron-silicon alloys at high pressure and high temperature. Physics and Chemistry of Minerals, 36, 511-518.

Li, B. S., and Liebermann, R. C. (2007), Indoor seismology by probing the Earth's interior using sound wave velocity measurements at high pressure and high temperatures. Proceedings of the National Academy of Sciences, doi:10.1073/pnas.0608609104.

Li, B. S., and Liebermann, R. C. (2014) Study of the Earth's interior using measurements of sound velocities in minerals by ultrasonic interferometry. Physics of the Earth and Planetary Interiors, 233, 135-153.

Lin, J. F., Campbell, A. J., Heinz, D. L., and Shen, G. Y. (2003b) Static compression of iron-silicon alloys: Implications for silicon in the Earth's core. Journal of Geophysical Research, 108(B1), 2045, doi:10.1029/2002JB001978.

Lin, J. F., Heinz, D. L., Campbell, A. J., Devine, J. M., and Shen, G. Y. (2002) Iron-Silicon Alloy in Earth's Core? Science, 295, 313-315.

Liu, J., Lin, J. F., Alatas, A., and Bi, W. L. (2014) Sound velocities of bcc-Fe and $Fe_{0.85}Si_{0.15}$ alloy at high pressure and temperature. Physics of the Earth and Planetary Interiors, 233, 24-32.

Lin, J. F., Struzhkin, V. V., Sturhahn, W., Huang, E., Zhao, J., Hu, M. Y., Alp, E. E., Mao, H. K., Boctor, N., and Hemley, R. J. (2003a) Sound velocities of iron-nickel and iron-silicon alloys at high pressures. Geophysical Research Letters, 30, doi:10.1029/2003GL018405.

Lin, J. F., Scott, H. P., Fischer, R. A., Chang, Y. Y., Kantor, I., and Prakapenka, V. B. (2009) Phase relations of Fe-Si alloy in Earth's core. Geophysical Research Letters, 36, L06306.

Lin, J. F., Sturhahn, W., Zhao, J., Shen, G., Mao, H, K., and Hemley, R. J. (2005) Sound velocities of hot dense iron: Birch's law revisited. Science, 308, 1892-1894.

Lin, Y. H., Tronche, E. J., Steenstra, E. S., and Westrenen, W. V. (2016) Evidence for an early wet Moon from experimental crystallization of the lunar magma ocean. Nature Geoscience, 10, 14-18, 2017.

Lv, J. N., Sun, Y. S., Toksoz, M. N., Zheng, Y., and Zuber, M. T. (2011) Seismic effects of the Caloris basin impact, Mercury. Planetary and Space Science, 59 (15), 1981-1991.

Malavergne, V., Toplis, M. J., Berthet, S., and Jones, J. (2010) Highly reducing conditions during core formation on Mercury: implications for internal structure and the origin of a magnetic field. Icarus, 206, 199-209.

Mao, Z., Lin, J. F., Liu, J., Alatas, A., Gao, L., Zhao, J., and Mao, H. K. (2012) Sound velocities of Fe and Fe-Si alloy in the Earth's core. Proceedings of the National Academy of Sciences, 109, 10239-10244.

Mao, H. K., Xu, J., Struzhkin, V. V., Shu, J., Hemley, R. J., Sturhahn, W., Hu, M. Y., Alp, E. E., Vočadlo, L., Alfè, D., Price, G. D., Gillian, M. J., Schwoerer-Böhning, M., Häusermann, D., Eng, P., Shen, G., Giefers, H., Lübbers, R., and Wortmann, G. (2001) Phonon density of states of iron up to 153 GPa. Science, 292, 914-916.

Mason, B. (1966) The Enstatite chondrites. Geochimica Cosmochimica Acta, 30, 23-39.

Massalski, T. B. (1986) Binary Alloy Phase Diagrams. American Society for Metals, Metals Park, 641 Ohio.

Mazarico, E., Genova, A., Goossens, S., Lemoine, F. G., Neumann, G. E., Zuber, M. T., Smith, D. E., and Solomon, S. C. (2014) The gravity field, orientation, and ephemeris of

Mercury from MESSENGER observations after three years in orbit. Journal of Geophysical Research, 119, 2417–2436, doi:10.1002/2014JE004675.

McCoy, T., Dickinson, T. L. and Lofgren, G. E. (1999) Partial melting of the Indarch(EH4) meteorite: A textural, chemical, and phase relations view of melting and melt migration. Meteoritics & Planetary Science, 34, 735-746.

Qin, L., Alexander, C. M. D., Carlson, R. W., Horan, M. F. and Yokoyama, T. (2010) Contributors to chromium isotope variation of meteorites. Geochimica Cosmochimica Acta, 74, 1122-1145.

Ricolleau, A., Fei, Y. W., Corgne, A., Siebert, J., and Badro, J. (2011) Oxygen and silicon contents of Earth's core from high pressure metal–silicate partitioning experiments. Earth and Planetary Science Letters, 310, 409-421.

Sanloup, C., Guyot, F., Gillet, P., Fiquet, G., Mezouar, M. and Martinez, I. (2000) Density measurements of liquid Fe-S alloys at high-pressure. Geophysical Research Letters, 27, 811-814.

Shen, G. Y., and Mao, H. K. (2017) High-pressure studies with x-rays using diamond anvil cells. Reports on Progress in Physics, 80, 016101.

Shibazaki, Y., NiShida, K., Higo, Igarashi, M. M., Tahara, M., SakaMaki, T., TeraSaki, H., ShiMoYaMa, Y., Kuwabara, S., Takubo, Y., and Ohtani, E. (2016) Compressional and shear wave velocities for polycrystalline bcc-Fe up to 6.3 GPa and 800 K. American Mineralogist, 101, 1150-1160.

Stark, A., Oberst, J., Preusker, F., Peale, S.J., Margot, J.-L., Phillips, R.J., Neumann, G.A., Smith, D.E., Zuber, M.T. and Solomon, S.C. (2015) First MESSENGER orbital observa-tions of Mercury’s librations. Geophysical Research Letters, 42 (19), 7881-7889.

519 Tsuchiya, T. (2003) First-principles prediction of the P-V-T equation of state of gold and the
520 660-km discontinuity in Earth's mantle. Journal of Geophysical Research, 108(1), 75-84.
521 Urick, R. J. (1947) A sound velocity method for determining the compressibility of finely
522 divided substances. Journal of Applied Physics, 18, 983-987.
523 Vocadlo, L., Wood, I. G., Gillan, M. J., Brodholt, J., Dobson, D. P., Price, G. D., Côté, D.,
524 Vocadlo, L., and Brodholt, J. P. (2008) The effect of silicon impurities on the phase diagram of
525 iron and possible implications for the Earth's core structure. Journal of Physics and Chemistry of
526 Solids, 69, 2177-2181.
527 Wänke, H., and Dreibus, G. (1997) New evidence for silicon as the major light element in the
528 Earth's core. Lunar and Planetary Science Conference XXVIII, 1280.
529 Warren, P. H. (2011) Stable-isotopic anomalies and the accretionary assemblage of the Earth and
530 Mars: a subordinate role for carbonaceous chondrites. Earth and Planetary Science Letters, 311,
531 93-100.
532 Weber, R. C., Lin, P. Y., Garnero, E. J., Williams, Q., and Lognonne, P. (2011) Seismic
533 detection of the lunar core. Science, 331, 309-312.
534 Whitaker, M. L., Liu, W., Liu, Q., Wang, L. P., and Li, B. S. (2009) Thermoelasticity of ε-FeSi
535 to 8 GPa and 1273 K. American Mineralogist, 94, 1039-1044.
536 Wieczorek M. A. (2006) The constitution and structure of the lunar interior. Reviews in
537 Mineralogy and Geochemistry, 60, 221-364.
538 Williams, Q. (2009) Bottom-up versus top-down solidification of the cores of small solar system
539 bodies: Constraints on paradoxical cores. Earth and Planetary Science Letter, 284, 564-569.

Yamada, A., Wang, Y. B., Inoue, T., Yang, W. G., Park, C. Y., Yu, T. and Shen, G. Y. (2011) High-pressure x-ray diffraction studies on the structure of liquid silicate using a Paris–Edinburgh type large volume press. Review of Scientific Instruments, 82, 015103.

Young, E. D., Kohl, I. E., Warren, P. H., Rubie, D. C., Jacobson, S. A., and Morbidelli, A. (2016) Oxygen isotopic evidence for vigorous mixing during the Moon-forming giant impact. Science, 351, 493-496.

Zhang, J., and Guyot, F. (1999) Thermal equation of state of iron and $Fe_{0.91}Si_{0.09}$. Physics and Chemistry of Minerals, 26, 206-211.

Zhang, J., Dauphas, N., Davis, A. M., Leya, I. and Fedkin, A. (2012) The proto-Earth as a significant source of lunar material. Nature Geoscience, 5, 251-255.

This is a preprint, the final version is subject to change, of the American Mineralogist (MSA)
Cite as Authors (Year) Title. American Mineralogist, in press.
DOI: https://doi.org/10.2138/am-2019-6564

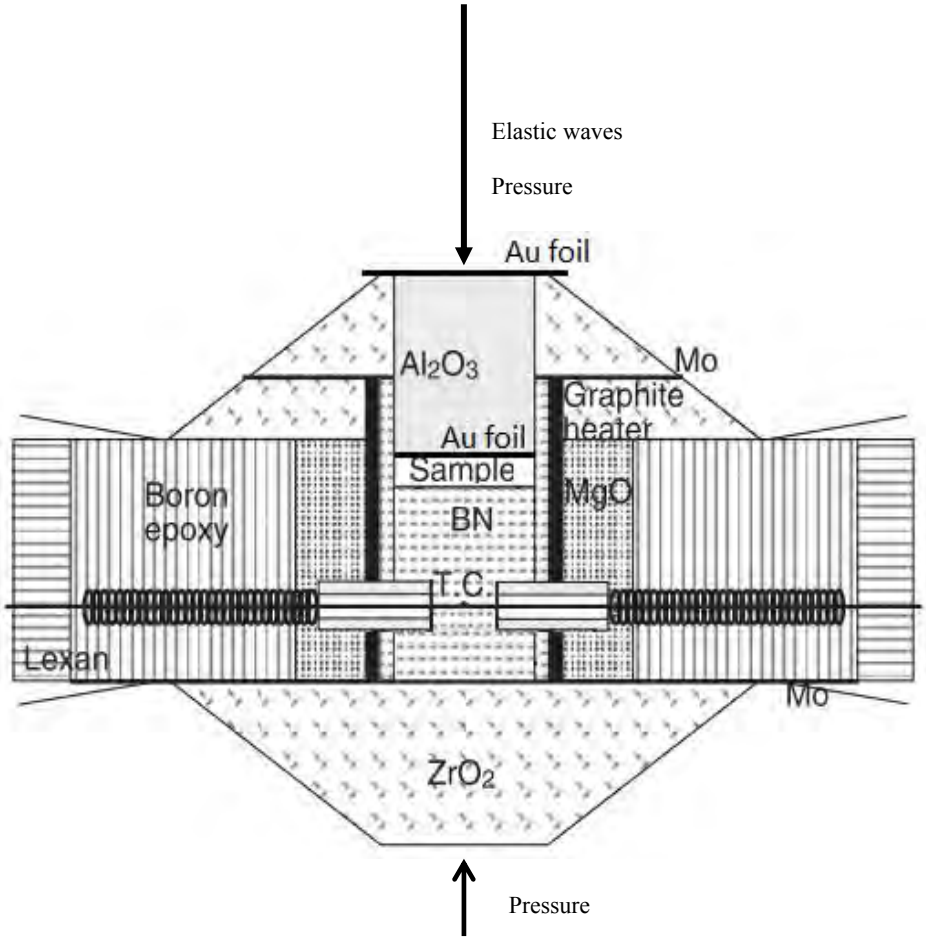

FIGURE 1. Schematic illustration of the cell assembly used in our high pressure and high temperature sound velocity measurements (modified from Kono et al., 2012). The top tungsten carbide (WC) anvil was used to generate 30MHz (for V_P) and 20MHz (for V_S) ultrasonic signals and to receive the reflected signals. Elastic waves passed through the WC anvil and propagated into an Al_2O_3 rod, the Fe_5Si sample and a BN rod. Reflected signals at the anvil/Al_2O_3 (R0), Al_2O_3/Fe_5Si sample (R_1) and Fe_5Si sample/BN (R_2) boundaries were recorded to calculate the travel time of V_P and V_S.

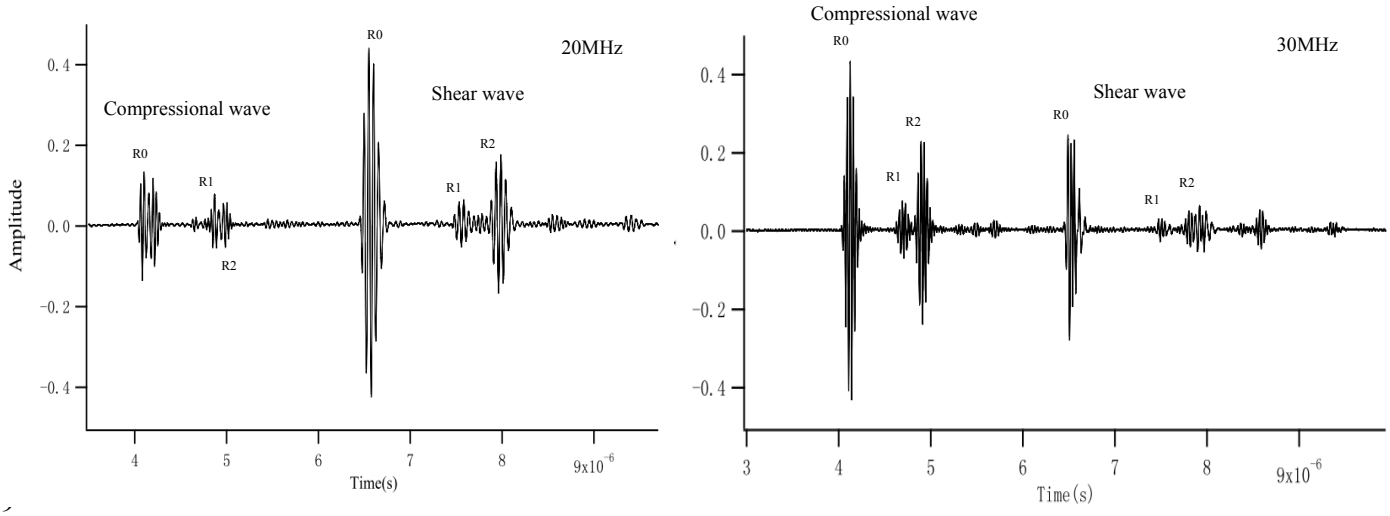

FIGURE 2. Examples of P- and S-wave signals obtained at 2.6 GPa and 985 K. The echoes from the R_1 and R_2 interfaces were clearly observed. The elastic wave travel time was determined by the pulse echo overlap method using the reflected signals from the R_1 and R_2 interfaces. This allowed us to precisely determine the travel time for both P- and S- waves (R_2-R_1 is travel time duration). The sample length under high P-T was measured from an X-ray radiography image using a high-resolution CCD camera. The pixel resolution was 0.948 μm/pixel. V_P and V_S were calculated by dividing the sample length by the travel time. Travel time durations and sample lengths were extracted using Igor software. More details can be found in Kono et al. (2012).

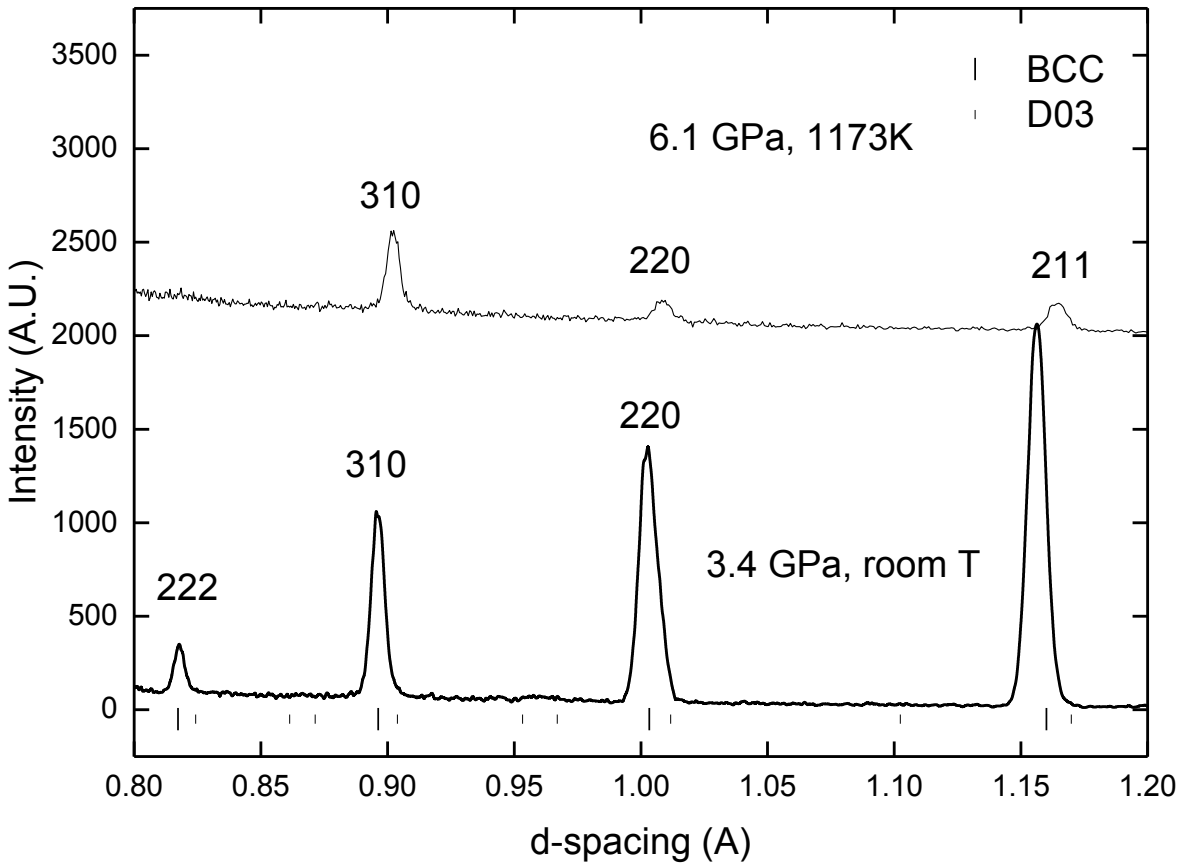

612
613

614 **FIGURE 3**. Diffraction patterns obtained from the bcc Fe_5Si sample at room temperature and
615 3.6 GPa and at 1173 K and 6.1 GPa. Structure measurements were carried out by energy-
616 dispersive x-ray diffraction with energy up to 150 keV. Diffracted x-rays were collimated to 0.5
617 mm × 0.2 mm (vertical × horizontal) with $2\theta = 15^{o}$ (Yamada et al., 2011). Standard bcc Fe and
618 $D0_3$ Fe_3Al structures at ambient condition are indicated. An obvious offset at high T pattern was
619 observed, which may due to crystal structure's relaxation upon heating.

620

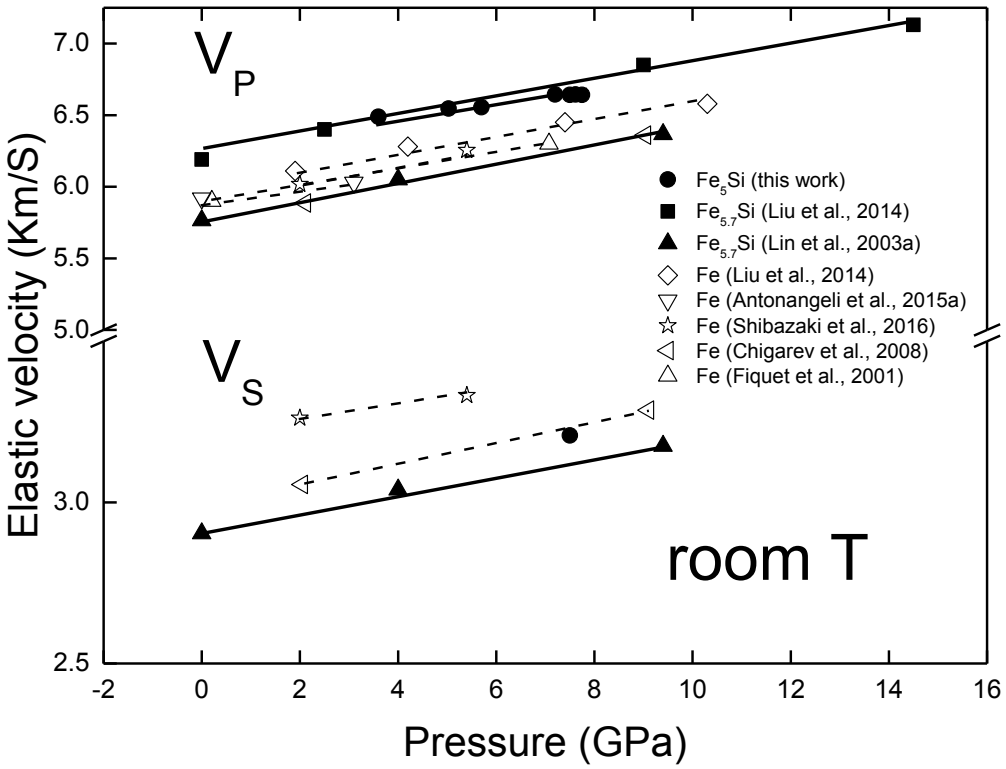

621
622

623 **FIGURE 4.** The effect of Si on V_P and V_S of bcc Fe at room temperature. Solid and empty
624 symbols represent Fe_5Si alloy and pure Fe, respectively. HERIXS was employed by Liu et al.
625 (2014) and Antonangeli et al. (2015a). NRIXS was employed by Lin et al. (2003). Ultrasonic
626 interferometry was adopted by Shibazaki et al. (2016) and this work. Laser ultrasonics was used
627 by Chigarev et al. (2008) and Fiquet et al. (2014). Lines are for vision guide only.

628

629

630

631

632

This is a preprint, the final version is subject to change, of the American Mineralogist (MSA)
Cite as Authors (Year) Title. American Mineralogist, in press.
DOI: https://doi.org/10.2138/am-2019-6564

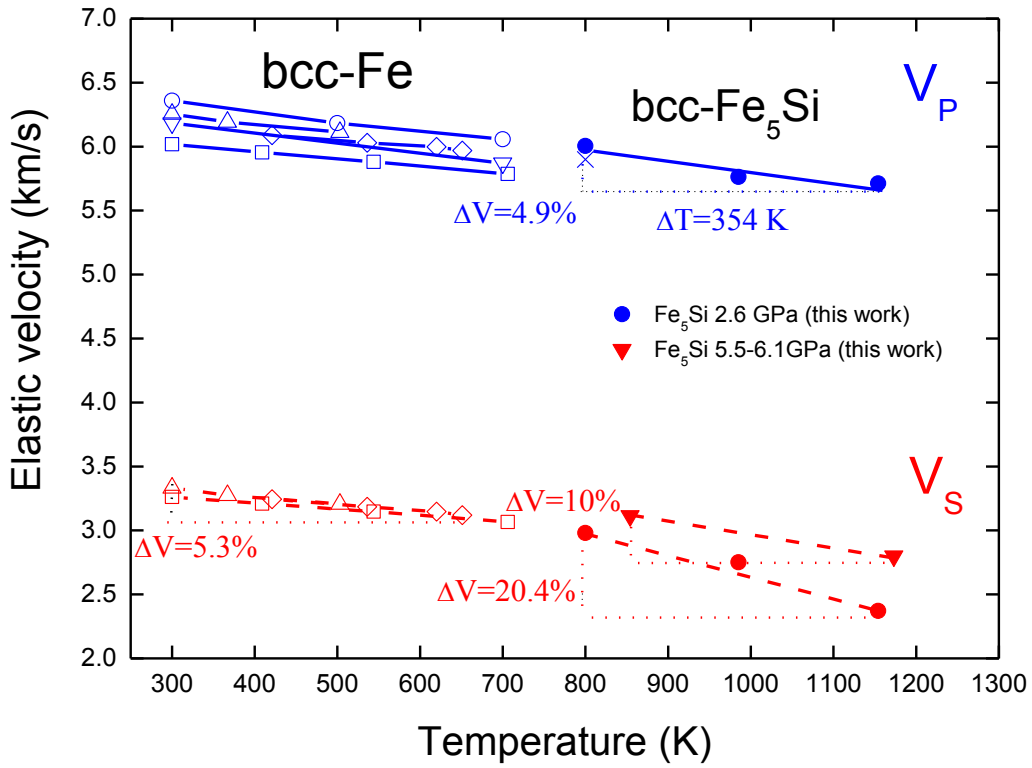

FIGURE 5. High P-T sound velocity of bcc Fe_5Si and Fe. Solid and empty symbols represent bcc Fe_5Si and Fe, respectively. V_P and V_S are represented by blue and red symbols, respectively. Empty down triangles and circles are HERIXS results at 3 GPa and 6 GPa, respectively (Liu et al., 2014). Cross is inelastic x-ray scattering data at 2.5 GPa (Antonangeli et al., 2015a). Empty squares, diamonds and upper triangles represent ultrasonic results at 2-2.7 GPa, 4-4.5 GPa and 5.4-5.8 GPa, respectively (Shibazaki et al., 2016).

643

644

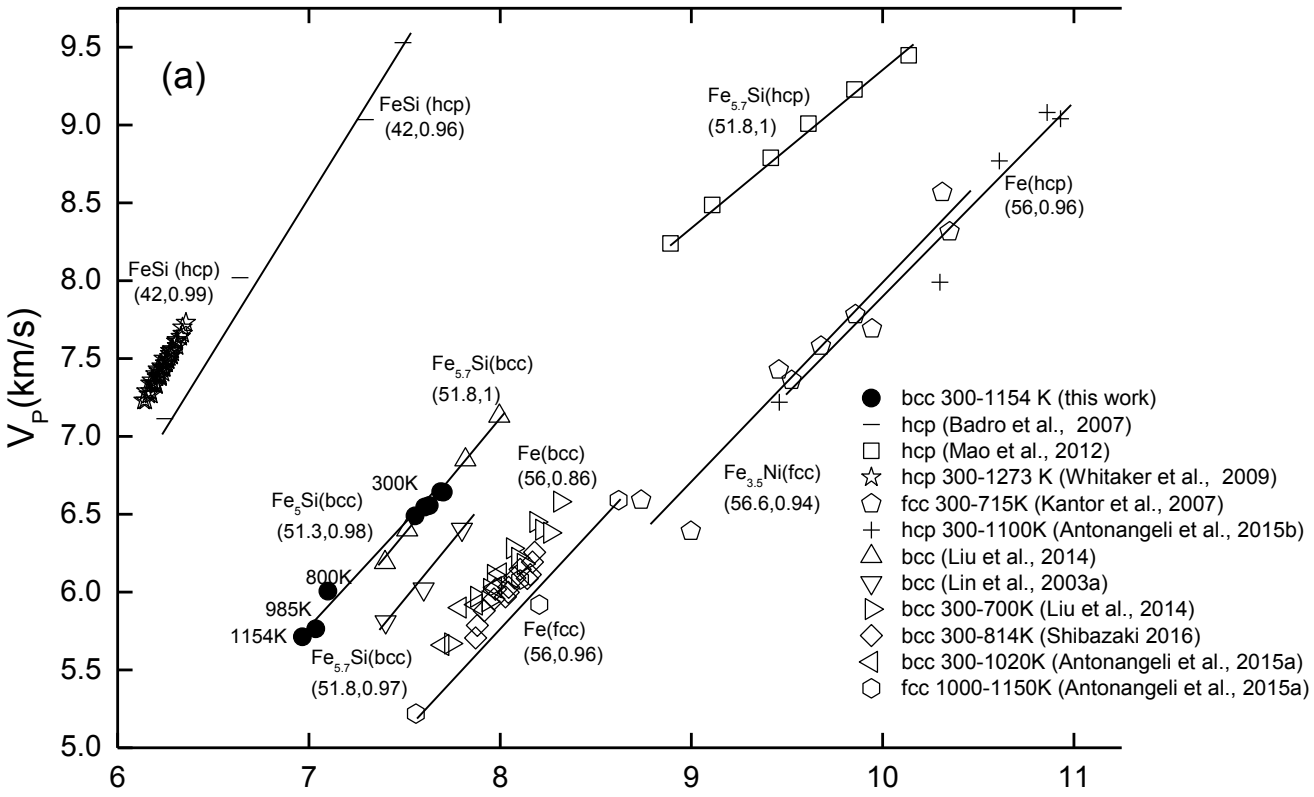

645

646

647

648

649

650

651

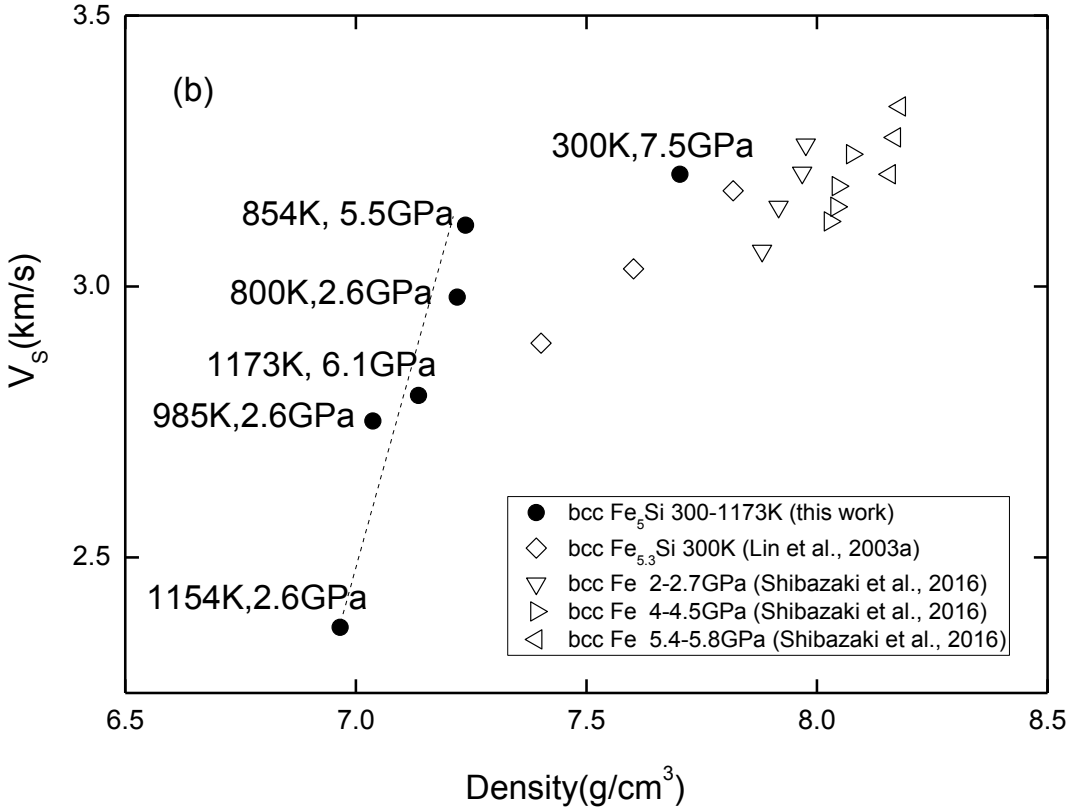

652 **FIGURE 6.** V-ρ relations of Fe and its alloys. Experimental conditions are given in the
653 legend. The experimental techniques employed in previous literatures are indicated as following.
654 Ultrasonic measurement: Whitaker et al. (2009) and Shibazaki et al. (2016). Inelastic x-ray
655 scattering: Badro et al. (2007), Kantor et al. (2007) and Antonangeli et al. (2010, 2015a, b).
656 HERIXS: Mao et al. (2012) and Liu et al. (2014). NRIXS: Lin et al. (2003). Our experimental
657 temperatures are labeled next to the symbols. (a) V_P-ρ relations. Numerical values in the brackets
658 are mean atomic weight and R^2 in linear regression, respectively. Except for three high
659 temperature data, our rest data were collected at ambient temperature. Unless specified otherwise
660 the V_P from previous literatures are at 300 K. (b)V_S- ρ relations. Our results are solid symbols
661 and empty ones are for previous literatures. V_S from Shibazaki et al. (2016) are at 300-814 K.
662 Our V_S-T data seems to follow a linear relation except for the 300 K. The dash lines are for eye
663 guide only.

This is a preprint, the final version is subject to change, of the American Mineralogist (MSA)
Cite as Authors (Year) Title. American Mineralogist, in press.
DOI: https://doi.org/10.2138/am-2019-6564

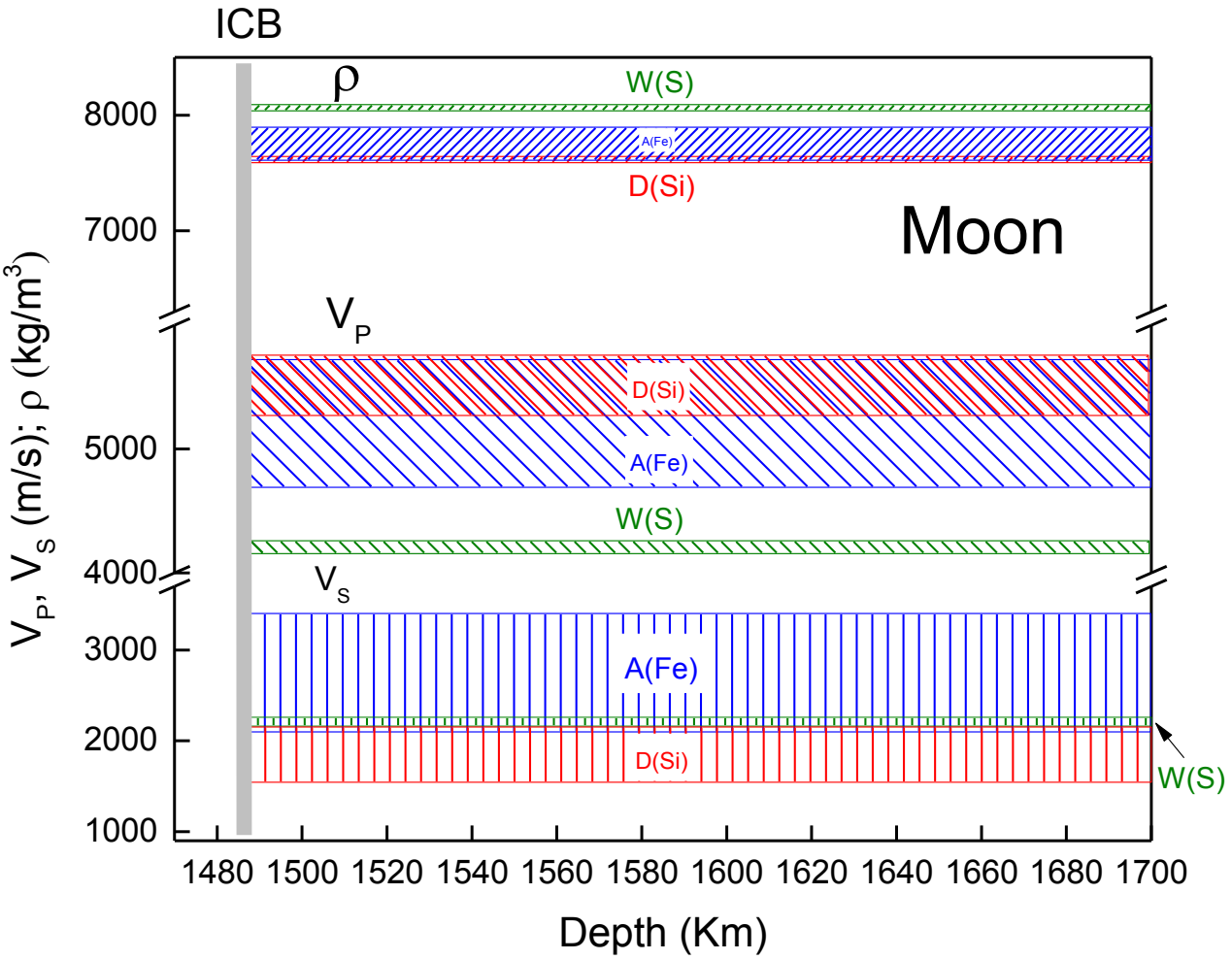

664 **FIGURE 7.** V_P, V_S and ρ model for lunar inner core. Vertical axis is divided into three
665 sections, which represent results of ρ, V_P and V_S, respectively. Left- and right-hand diagonals
666 are V_P and ρ, respectively. Vertical lines are V_S. Blue, green and red represent results from
667 Antonangeli et al., (2015a) (A), Weber et al., (2011) (W) and this work (D). Our profiles were
668 calculated at 5 GPa, 1300 K and 1900 K. Elements in the bracket represent studied light element
669 in literatures. Grey line marks the solid inner core boundary.

670

671

This is a preprint, the final version is subject to change, of the American Mineralogist (MSA)
Cite as Authors (Year) Title. American Mineralogist, in press.
DOI: https://doi.org/10.2138/am-2019-6564

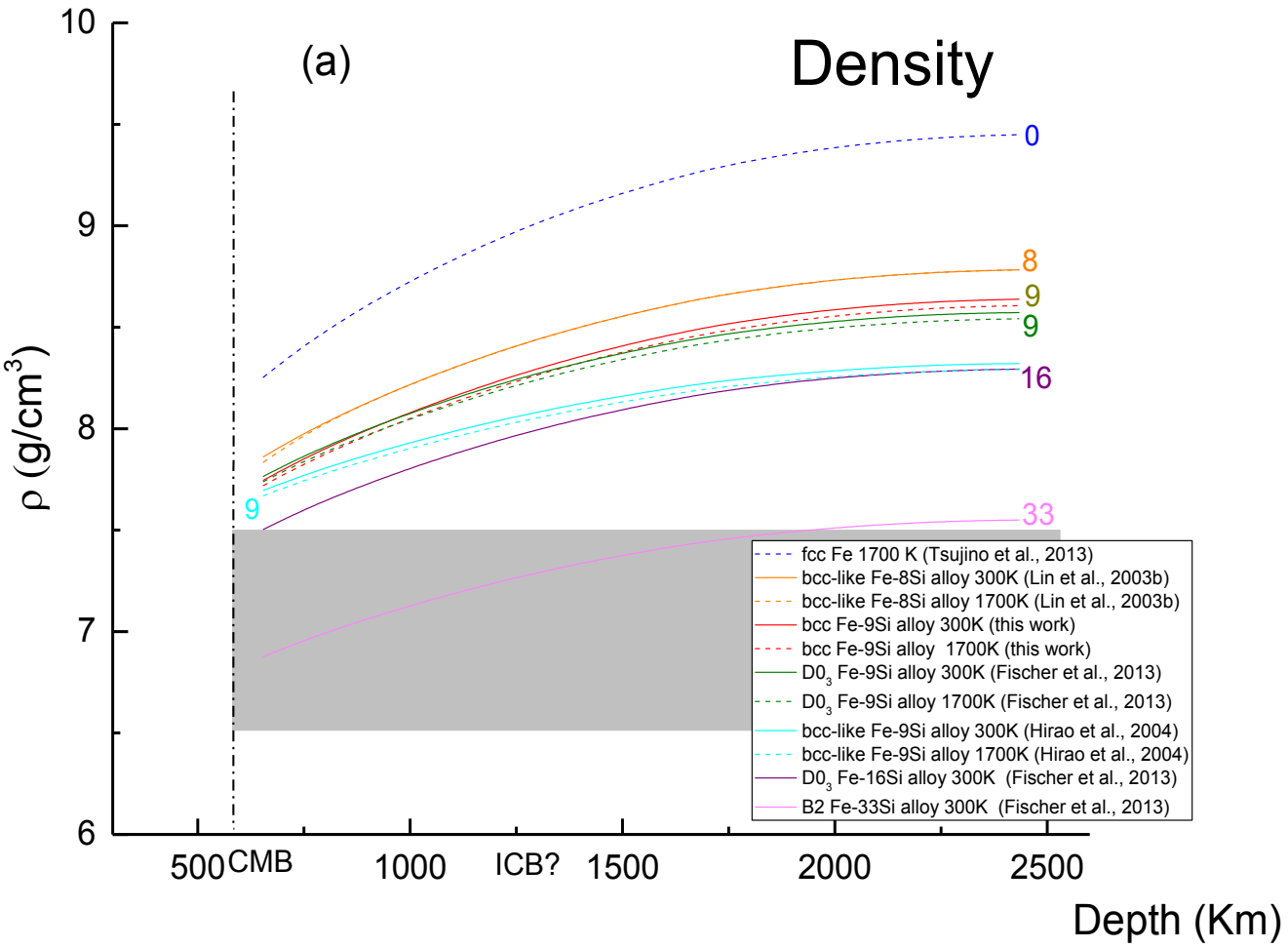

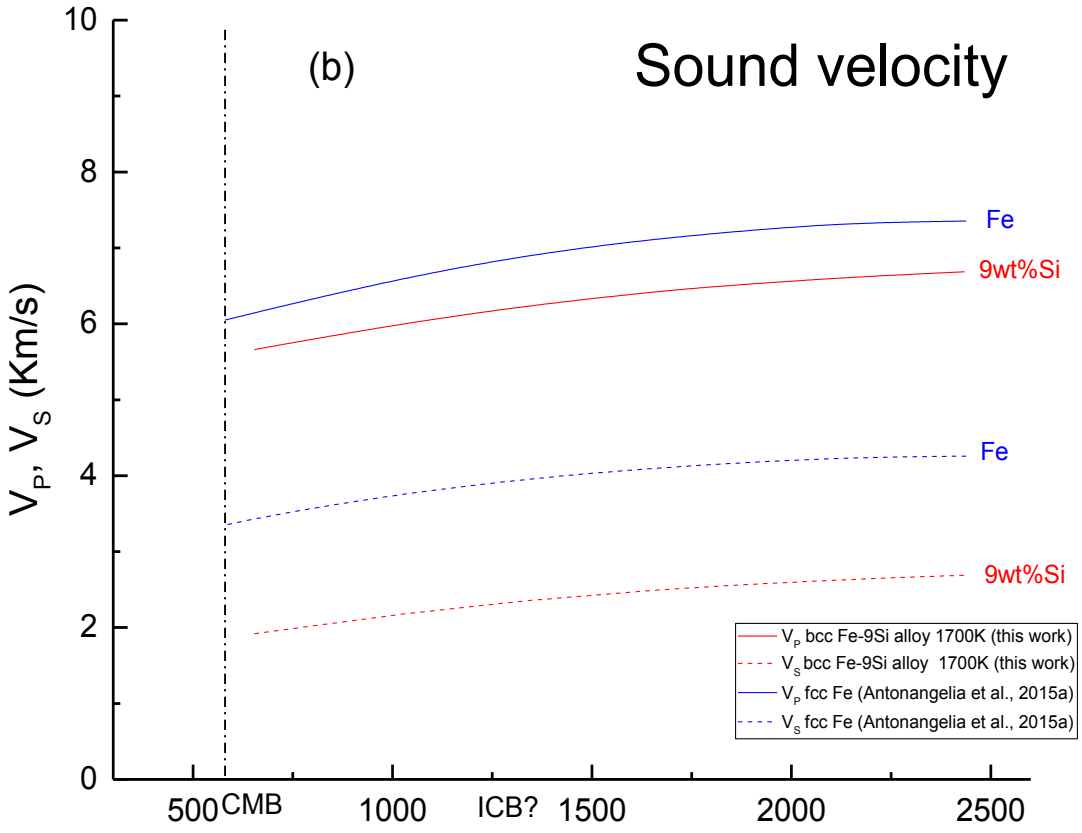

FIGURE 8. Density (a) and sound velocity (b) profiles at Mercury's core conditions. Pressure-depth relation of Mercurian core is from seismic structure model reported by Lv. (2011). CMB marks the core-mantle boundary. Mercurian core might be partially molten. However, ICB depth has not been well defined yet. In (a), the shade area shows the densities range of a Si-bearing Mercurian core which satisfies observed C/MR^2 and C_m/C values by radio tracking data from the MESSENGER spacecraft (Knibbe and Westrenen 2018). The numbers labeled besides the symbols represent Si content in Fe-Si alloy applied in literatures. The $D0_3$ structure is an ordered version of the B2 structure, which is an ordered version of the bcc structure. In (b), Lv's sound velocity profiles were calculated based on mineral physics data assuming temperature is 1825 K at CMB. Sound velocities profiles of fcc iron are from linear sound velocity-density relation reported by Antonangeli et al. (2015a). It clearly shows incorporating Ni in pure Fe results in an increased sound velocity while adding Si has the opposite effect.

This is a preprint, the final version is subject to change, of the American Mineralogist (MSA)
Cite as Authors (Year) Title. American Mineralogist, in press.
DOI: https://doi.org/10.2138/am-2019-6564

718

719

720 **TABLE 1.** Experimental conditions and results of sound velocity measurements.

721

722

723

Run No.	P (GPa)	T (K)	V_P (km/s)	V_S (km/s)	ρ (g/cm^3)
1	3.6(3)	300	6.49(1)		7.56(2)
1	5.0(3)	300	6.55(1)		7.61(1)
1	5.7(3)	300	6.56(1)		7.63(1)
1	7.2(3)	300	6.64(1)		7.69(0)
1	7.5(6)	300	6.64(1)	3.21(3)	7.70(0)
2	2.6(1)	800	6.01(2)	2.98(4)	7.10(1)
2	2.6(2)	985	5.76(2)	2.75(4)	7.04(2)
2	2.6(2)	1154	5.71(2)	2.37(3)	6.97(1)
2	5.5(5)	854		3.11(4)	7.24(0)
2	6.1(1)	1173		2.80(4)	7.14(2)

724

725

726

727

728

729

730

731

732

733

734

735